Title: CIT tumor lines: A novel series of immunogenic cutaneous squamous cell carcinoma cell lines derived from chemical carcinogenesis

Authors

Robert Letchworth[1,2,*], Miho Tanaka[3,*], Alina A Barnes[1,2], Lotus Lum[3], Savannah Hughes[1], Grant Schlauderaff[1], Piyush Chaudhary[1,2], Kenneth M Ng[3], Daphne Superville[3], Corinna Martinez Luna[3], Maria Gonzalez[3], Dekker C Deacon[1,4], Allie Grossmann[5], Melissa Q Reeves[1,2]

Affiliations

[1]Huntsman Cancer Institute, University of Utah

[2]Department of Pathology, University of Utah

[3]Department of Microbiology and Immunology, University of California, San Francisco

[4]Department of Dermatology, University of Utah

[5]Earle A. Chiles Research Institute, Providence Cancer Institute of Oregon, Portland, OR

[*]These authors contributed equally.

Correspondence: melissa.reeves@hci.utah.edu

Keywords

Cutaneous squamous cell carcinoma, tumor immunology, tumor neoantigen, immune checkpoint inhibitor, mouse models of cancer

Abstract

Immunotherapy is now widely used to treat advanced-stage skin cancer, but it is effective for only approximately half of skin cancer patients, including both patients with melanoma and cutaneous squamous cell carcinoma (cSCC). To overcome current barriers, preclinical mouse models that faithfully recapitulate the tumor genetics, mutation burdens, and neoantigen patterns of specific human tumor types are essential. However, while many models exist for melanoma, there are currently relatively few transplantable murine models of cSCC, which is responsible for nearly as many deaths as melanoma each year. Here we describe a novel series of 11 cSCC tumor lines, the Carcinogen-Induced Tumor (CIT) lines, syngeneic to the FVB strain, that address this need. The CIT lines were established from skin carcinomas induced by DMBA and TPA treatment and harbor genetic drivers and overall tumor mutational burdens that recapitulate those found in cSCC. Each CIT line gives rise to tumors with a consistent immune infiltration pattern, ranging from T cell-rich “hot” tumors to T cell-poor “cold” tumors. Hot CIT lines exhibit partial responses to treatment with immune checkpoint inhibitors, and we have identified two neoantigens present in an immunotherapy-responsive CIT line. The CIT lines thus provide a valuable new series of preclinical models for studying anti-tumor immune responses and developing strategies to improve immunotherapy efficacy in cSCC.

Background

45 Cutaneous squamous cell carcinoma (cSCC) is the second most common cancer type in
46 the United States, affecting approximately 700,000 people annually[1–3] and responsible for
47 between 8,000 and 15,000 deaths per year[1,4]. Although cSCC carries a relatively low risk of local
48 advancement or distant metastasis, its high incidence rate means that as many or more
49 Americans are estimated to die every year from cSCC as from melanoma[4]. Among high-risk
50 cSCC patients, up to 5% will progress to locally advanced or metastatic tumors that cannot be
51 treated with surgery or radiation alone[1,5,6]. Immune checkpoint inhibitors (ICIs), which have
52 revolutionized cancer treatment over the past decade[7,8], are approved for advanced cSCC, and
53 hold immense potential to be curative for these patients[9,10]. However, overall response rates of
54 cSCC to ICI therapy are only 50-60% in locally advanced disease[10–12] and drop as low as 35% in
55 metastatic disease[11]. These statistics highlight an unmet clinical need to understand why ICI
56 fails for many cSCC patients and how immunotherapy strategies can be improved for these
57 patients[10–13].
58 Murine models play a vital role in basic and translational cancer research, providing a
59 means of conducting mechanistic experiments to dissect cancer and immune cell biology and
60 their interactions with therapy. Transplantable tumor models, in which cancer cell lines are
61 implanted into immune-competent syngeneic hosts, play a particularly important role in
62 preclinical research, as the reliability of their growth kinetics makes them a workhorse for
63 testing the efficacy of new therapies or combinations. Additionally, transplantable murine
64 models are essential for studying immunotherapy. Because ICIs primarily act directly on T cells,
65 they are effective only in immune-competent hosts, making patient-derived xenografts
66 (PDXs)—which grow only in mice with compromised immune systems—unsuitable models to

67 study immunotherapy. However, while transplantable murine models of melanoma are widely
68 available and have contributed to substantial advancements in immunotherapy, relatively few
69 transplantable tumor models are available for cSCC. Many barriers to the efficacy of
70 immunotherapy are cancer type-specific, and there is a need for mouse models that accurately
71 recapitulate the unique features of each disease. As such, the lack of availability of
72 transplantable cSCC models represents a significant gap in the field.

73 Here we describe the Carcinogen-Induced Tumor (CIT) cell line panel, a novel series of
74 murine cSCC cell lines, to address this need. The CIT lines are derived from DMBA/TPA-induced
75 cutaneous SCCs, and they are syngeneic to the FVB strain. Notably, the CIT cell lines
76 recapitulate the mutational profiles of human cSCC, including harboring cSCC-relevant driver
77 mutations in *Hras* and *Trp53* and deletions of *Cdkn2a*. As a result of being chemically induced in
78 immune-competent hosts, the CIT lines carry a moderate to high mutation burden, like human
79 cSCC[14,15]. The tumors that arise from the CIT lines exhibit a range of reproducible patterns of
80 immune infiltration—from high to low T cell infiltrate—along with a corresponding range of
81 responses to immunotherapy. Additionally, as a consequence of their high mutation burden,
82 the CIT lines harbor endogeneous neoantigens, which are mutant proteins—resulting from
83 genetic mutations—that can be recognized by T cells[8]. Neoantigens enable T cells to identify
84 tumor cells as "foreign," and this recognition is a critical central mechanism of the anti-tumor
85 immune response that is enhanced by ICI therapy[8,16]. The presence of these neoantigens—two
86 of which we describe in this manuscript—are an additional valuable tool to facilitate the study
87 of tumor-specific T cells during immunotherapy responses in cSCC.

88 The CIT cell line series thus offers a panel of cSCC tumor models that exhibit a range of
89 mutational burdens, immune infiltrates, and neoantigens, while being driven by cSCC-relevant
90 genomic drivers and exhibiting histopathologic features characteristic of cSCC. These properties
91 make the CIT lines a valuable set of preclinical models for investigating tumor biology and
92 responses to therapy, particularly immunotherapy, in cSCC.
93
94 **Results**
95
96 **CIT lines display a range of reproducible immune infiltration phenotypes.**
97 The CIT cell lines were derived from skin carcinomas that arose by topically treating *K5-*
98 *CreER^{T2}-Confetti* FVB/N mice with a single dose of 7,12-dimethylbenzanthracene (DMBA)
99 followed by 12-O-tetradecanoylphorbol-13-acetate (TPA) twice weekly for 20 weeks, using a
100 well-established skin carcinogenesis protocol[17,18] (**Fig. 1A**). In the DMBA/TPA model, benign
101 papillomas arise after about 6 weeks of TPA treatment, and approximately 10% of these
102 progress to malignant carcinomas. Primary carcinomas were resected when they were
103 approximately 1cm in longest diameter, digested into a single cell suspension, and grown under
104 standard tissue culture conditions. Each cell line was established in tissue culture for >10
105 passages. Implantation of 1.25×10^5 tumor cells into the subcutaneous flank of FVB mice gave
106 rise to tumors with 100% penetrance, and we subsequently profiled the histopathologic and
107 immune characteristics of these tumors.
108 We carried out immune profiling of 11 CIT cell lines by flow cytometry, quantifying the
109 number of total T cells, CD4+ and CD8+ T cells in tumors from each CIT model (**Supp. Fig. 1A**).

110 We found each CIT line gave rise to tumors with a consistent pattern of immune infiltration,
111 spanning the range of immune "hot" (highly infiltrated by T cells, e.g., CIT18) to immune "cold"
112 (poorly infiltrated by T cells, e.g., CIT9) (**Fig. 1B**). Interestingly, we observed a consistent bias in
113 the T cell compartment toward CD4+ T cells, about half of which were Tregs (**Supp. Fig. 1B**). We
114 selected 5 CIT lines, including representation of both hot and cold models, for more extensive
115 immune profiling. On the whole, we found the myeloid compartment of CIT tumors was
116 strongly biased toward macrophages (CD11b+MHCII+F4/80+), with relatively fewer Ly6C+ and
117 Ly6G+ myeloid cells (monocytes and neutrophils, respectively) and DCs (CD11c+MHCII+) (**Fig.**
118 **1C, Supp. Fig. 1A**). Macrophage infiltration was highest in the two coldest (lowest T cell
119 infiltrate) CIT models, CIT22 and CIT9. Conversely, hot models CIT18 and CIT6 exhibited the
120 highest B cell infiltration (**Fig. 1C**). There was no clear trend between hot and cold tumors for
121 $Ly6G^{hi}Ly6C^{mid}$ neutrophils, $Ly6C^{hi}$CD11b+ monocytes, or CD11c+MHCII+ dendritic cells (**Fig. 1C**).
122 Tumor histology for the same five selected CIT tumor models was reviewed by a board-
123 certified pathologist. Tumors from all five CIT models were poorly differentiated, spindled,
124 arranged in fascicles, and highly mitotic (**Fig. 1D**). Some CIT18 tumors contained pleomorphic,
125 rhabdoid, or epithelioid malignant cell morphologies. Among the hot models, CIT18 and CIT17
126 tumors contained brisk tumor-infiltrating lymphocyte (TIL) infiltration, while CIT6 tumors
127 contained focal clusters of TILs or TILs localized to the edge of the tumor. In comparison,
128 tumors arising from the cold lines CIT9 and CIT22 displayed very little TIL infiltration. CIT6,
129 CIT17, CIT18 and CIT22 tumors contained diffuse infiltration of polymorphonuclear (PMN) cells,
130 while PMNs in cold CIT9 tumors were largely restricted to the edge of the tumors. Altogether,
131 we find that the CIT cell lines give rise to tumors that recapitulate the histologic features of high

132 grade, sarcomatoid SCC, and each exhibits characteristic patterns of immune infiltration
133 congruent with flow cytometry-based immune profiling.
134
135 **Genomic profiles of CIT lines recapitulate human SCC.**
136 All 11 CIT cell lines were subjected to exome sequencing, to a median depth of 153X.
137 Consistent with previous sequencing of DMBA/TPA tumors by ourselves and others[17,19,20], CIT
138 cell lines were genomically characterized by *Hras* driver mutations, *Cdkn2a* losses, a substantial
139 mutation burden, and whole-chromosome copy number alterations. The mutation burden
140 among the CIT lines ranged from 174 to 703 mutations (5.2-21.0 mutations/Mb; average of 10
141 mutations/Mb), including 46 to 256 non-synonymous mutations (**Fig. 2A-B, Supp. Table 1**). Ten
142 of our CIT lines exhibited an *Hras* Q61L mutation, while one, CIT16, exhibited an *Hras* G12V as
143 well as a *Kras* G13R mutation (**Fig. 2C**). Seven CIT lines displayed additional non-synonymous
144 mutations in driver genes known to be mutated in human cSCC, including *Trp53* and *Fgfr3*,
145 while nine CIT lines harbored a deletion at the *Cdkn2a* locus (**Fig. 2C**). The majority of total
146 mutations were T>A transversions, with a particular prevalence of CTN>A mutations (with N
147 representing any nucleotide) consistent with the known mutagenic signature of DMBA[17,19,20]
148 **(Fig. 2D)**. While this signature is not identical to the C>T mutations induced by UV and typically
149 found in cSCC[14,15], we note that the genes mutated in the CIT lines were nonetheless cSCC-
150 relevant driver genes, including mutations at classical *Hras* hotspots in codons 12 and 61. The
151 CIT lines also harbored whole-chromosome alterations, primarily amplifications, especially on
152 chromosomes 6 and 15 **(Fig. 2E)**. Chromosome 6 amplifications are common in DMBA/TPA-
153 induced skin carcinomas[17]. Chromosome 15 amplifications were also previously observed, but

154 they were more heavily represented in the CIT lines than in a previously sequenced cohort of
155 primary tumors[17], suggesting perhaps a selection in cell culture for lines with this amplification.
156 Interestingly, we saw only one whole-chromosome amplification each of chromosome 1 and
157 chromosome 7. We previously reported that chromosome 1 and 7 amplifications are common
158 in DMBA/TPA carcinomas with an epithelial-like "squamous" morphology, but largely absent in
159 DMBA/TPA carcinomas with a mesenchymal-like "spindle" morphology[17]. The
160 underrepresentation of these alterations is perhaps not surprising given that the CIT lines
161 primarily give rise to tumors with spindle cell morphology, but may again suggest a selection
162 bias of the cell lines we were able to establish in culture.
163 Given that mutation burden information and immune phenotypes were available for all
164 11 cell lines, we examined whether a relationship existed between these metrics. While two of
165 the tumors with the highest T cell infiltration, CIT18 and CIT6, exhibited two of the three
166 highest mutation burdens, we observed that tumor model with the second-highest T cell
167 infiltration, CIT16, had a relatively low mutation burden. CIT23 tumors, which had the second-
168 highest mutation burden, were by contrast very poorly infiltrated by T cells. Thus, aligning with
169 observations from patients, mutation burden alone was insufficient to predict the immune
170 response to any given tumor, and there was not a significant correlation between mutation
171 burden and T cell infiltrate across CIT models (**Fig. 2F**).
172
173 **Immunologically hot CIT lines respond to immunotherapy.**
174 Because our CIT lines exhibited moderate to high tumor mutation burdens, we
175 hypothesized they would carry neoantigens and would be sensitive to immune checkpoint

176 inhibitors (ICIs). We tested the efficacy of a combination ICI regimen—anti-PD-1 plus anti-CTLA-
177 4, administered as two doses 3 days apart—on CIT18, CIT6, and CIT9 tumors (**Fig. 3A**).
178 CIT18 and CIT6 tumors—both of which we had observed to be immunologically hot—
179 grew significantly slower than controls when treated with anti-PD-1 plus anti-CTLA-4 (hereafter,
180 "ICI") **(Fig. 3B)**. Conversely, immunologically cold CIT9 tumors displayed no difference in growth
181 between ICI-treated and control tumors **(Fig. 3B)**. We carried out immune profiling of ICI- and
182 control-treated tumors to interrogate how ICI remodeled the immune response in these
183 models. CIT18 tumors had the strongest response to ICIs, both in terms of the reduction in
184 growth and in the increase in tumor infiltrating T cells. Total T cells, CD8+ T cells and CD4+ T
185 cells were all more abundant in ICI-treated CIT18 tumors (**Fig. 3C**, **Supp. Fig. 2A**). CIT6 tumors,
186 which showed a more modest response to ICI than CIT18, only exhibited an influx of CD8+ T
187 cells following ICI, while CIT9 tumors showed no increase in overall T cell infiltration. **(Fig. 3D-E**,
188 **Supp. Fig. 2A)**.
189 ICI treatment also altered the activation profile of tumor-infiltrating T cells. Effective ICI
190 treatment in CIT18 and CIT6 tumors was accompanied by an increase in the percentage of CD8+
191 and CD4+ T cells which exhibited a CD44+CD62L- "effector-like" phenotype **(Fig. 3F-G**, **Supp.**
192 **Fig. 2B).** Notably, in hot tumors this increase in "effector-like" CD8+ T cells resulted in a skewing
193 of the CD8+ compartment away from a CD44+CD62L+ "central memory-like" phenotype, even
194 though the abundance of central memory-like CD8+ T cells as a percent of all immune cells was
195 unchanged **(Supp. Fig. 2C)**. In contrast, ICI treatment in cold CIT9 tumors was unsuccessful at
196 shifting the phenotype of either CD8+ or CD4+ T cells **(Fig. 3H**, **Supp. Fig. 2B-C)**. We further
197 examined the expression of PD-1, which is present on both activated and exhausted T cells, and

198 Tim3 and TIGIT, both of which mark exhaustion, on CD8+ T cells. The proportion of tumor-
199 infiltrating CD8+ T cells expressing PD-1 increased after ICI treatment in all three tumor models
200 **(Fig. 3I-K)**. Interestingly, the "activated" PD-1+Tim3-TIGIT- T cell population was the primary
201 CD8+ population to increase in CIT18 tumors following ICI **(Fig. 3I, Supp. Fig. 2D)**, and this
202 corresponded to the best tumor growth control. By contrast in CIT6 tumors, which showed
203 more modest tumor growth control, the proportion of "activated" PD-1+Tim3-TIGIT- CD8+ T
204 cells did not increase as a fraction of PD-1+ CD8+ T cells **(Fig. 3J)**. Instead, there was an increase
205 in the proportion of PD-1+ CD8+ T cells with an exhausted (PD-1+Tim3+ or PD-1+Tim3+TIGIT+)
206 phenotype after ICI treatment **(Supp. Fig. 2D)**. Together, this data shows that CIT tumor models
207 exhibit a range of responses to immunotherapy, and that the degree of sensitivity appears to
208 be approximately correlated with the level of T cell infiltration in untreated tumors.
209
210 **CIT tumors display identifiable and immunotherapy-sensitive neoantigens.**
211 Cytotoxic CD8+ T cells recognize tumor cells by using their T cell receptor (TCR) to detect
212 neoantigens, which are fragments of mutant proteins that arise from genetic mutations in the
213 tumor[8,16], and which allow T cells to see tumor cells as "foreign." Given that improvement in
214 the CD8+ T cell response corresponded to effective tumor control following ICI, we next sought
215 to identify the neoantigens recognized by CD8+ T cells during this response. We focused here
216 on the CIT6 tumor model, which exhibited the intermediate response to ICI among the three
217 models tested and thus may be most representative of patient tumors which are recognized by
218 the host immune response but benefit only marginally from current ICI strategies. We
219 employed the NetH2pan algorithm[21] to predict the binding strength between the H2-D^q and H2-

220 K^q MHCI alleles carried by FVB/N mice and the neoepitopes predicted to be generated by all
221 non-synonymous mutations identified in our exome sequencing analysis. We identified 27 top
222 binders, and these were further filtered to prioritize those for which the mutant sequence was
223 predicted to exhibit better binding than the wild-type sequence, and for which we could detect
224 expression of the gene by RNAseq (**Fig. 4A-B**, **Supp. Table 2)**.

225 Candidate neoantigens identified through this pipeline were subsequently screened by
226 *in vitro* IFNγ ELISPOT assay[22,23]. Whole splenocytes, CD8+ T cells, or CD4+ T cells from the spleen
227 of CIT6 tumor-bearing mice were incubated with synthetic peptides corresponding to each
228 candidate epitope sequence (**Fig. 4C**). We identified two peptides, CPAFLPCTV (resulting from a
229 Brinp3 T436P mutation) and VPPSSLLPL (resulting from a Ttll4 Q454L mutation), which
230 consistently elicited IFNγ production in sorted CD8+ T cells from CIT6-bearing mice in a peptide
231 concentration-dependent manner (**Fig. 4D-G**). These peptides elicited no response from sorted
232 CD4+ T cells (**Supp. Fig. 3A**). When the peptide assay was carried out with whole splenocytes
233 (no prior sorting of CD8+ or CD4+ T cells), the dose-dependent response to VPPSSLLPL (Ttll4
234 Q454L mutation) was still observed, but the response to CPAFLPCTV (Brinp3 T436P mutation)
235 was not detectable above background (**Supp. Fig. 3B**).

236 We next interrogated the effect of ICI therapy on the T cell response to VPPSSLLPL,
237 focusing on VPPSSLLPL because its response was more clearly detected in whole splenocytes
238 **(Supp. Fig. 3B)**. CIT6 tumors were treated with three doses of anti-PD-1 and anti-CTLA-4
239 combination therapy (**Fig. 4H**), and an IFNγ ELISPOT assay was carried out on whole splenocytes
240 harvested 3 days after the final dose of ICI. Splenocytes from ICI-treated mice produced a
241 robust IFNγ response when incubated with VPPSSLLPL compared to no peptide **(Fig. 4I)**,

242 indicating that response to the neoantigen VPPSSLLPL is prominent during immunotherapy
243 response.
244
245 **Discussion**
246 We have established the CIT lines as a novel series of *Hras*-driven cSCC tumor lines, and here
247 present comprehensive histologic, genomic, and immune characterization of these 11 cell lines.
248 The CIT lines carry genomic drivers relevant to human cSCC, as well as a moderate-to-high
249 mutation burden[14,15]. We show that each CIT line exhibits a characteristic immune infiltrate,
250 with individual cell lines ranging from immune hot to immune cold. Immune hot CIT lines CIT6
251 and CIT18 exhibit partial responses to an immunotherapy regimen of anti-CTLA-4 and anti-PD-1.
252 We have also identified two neoantigens that elicit CD8+ T cell responses in the CIT6 cell line. Of
253 note, while numerous neoantigens have been identified in tumor models syngeneic to
254 C57BL/6[22–26], there has been a notable dearth of neoantigen identification in other mouse
255 strains including FVB, as well as a lack of neoantigens identified in cSCC models. The CIT lines,
256 with the identification of two MHCI-restricted neoantigens in CIT6, thus provide a valuable new
257 series of models for immunotherapy research in cSCC.
258 As noted above, the CIT cell lines are syngeneic to FVB mice. This stands in contrast to
259 the majority of mouse models currently used for immunotherapy studies—across all cancer
260 types—which are syngeneic to C57BL/6 mice. C57BL/6 mice are known to have a Th1-biased
261 immune response[27]. While this is likely beneficial for tumor control—and C57BL/6 mice are
262 widely known for their resistance to tumorigenesis[28,29]—it is not necessarily representative of
263 the diversity of human immune responses. FVB mice, in contrast to C57BL/6, are known to

264 exhibit Th2-biased immune responses[27,30] and to be readily susceptible to tumorigenesis. While
265 no single mouse model or mouse strain can represent the full spectrum of human immunity,
266 increasing the diversity of mouse strains used to model anti-tumor immune responses is
267 essential to capture human diversity and understand the full spectrum of barriers to
268 immunotherapy success that are found in patients.

269 Finally, an additional feature of the CIT lines, having been derived from *K5CreER*^{T2}-
270 *Confetti* mice, is that cells can be labeled with fluorescent tags following exposure to Cre
271 recombinase[31,32]. We have successfully labeled CIT lines *in vitro* using adenoviral Cre
272 recombinase. While the *K5CreER*^{T2} allele will also allow for labeling of K5+ (Keratin 5+) cells
273 following tamoxifen treatment, we have found low expression of K5 in these poorly
274 differentiated cell lines—as well as in DMBA/TPA tumors following progression to the
275 carcinoma stage[31]—making this approach less effective. Introducing Cre and subsequently
276 sorting cells enables the establishment of isogenic cell lines with each GFP, YFP, RFP or CFP[32];
277 while introducing Cre to activate labeling without sorting could allow for multiclonal lineage
278 tracing.

279 Improving immunotherapy outcomes in advanced cSCC remains an unmet clinical need.
280 The CIT panel of cutaneous SCC tumor lines provides an important new set of tools to better
281 understand the mechanisms behind immunotherapy resistance in cSCC, and to preclinically
282 model novel approaches to overcoming ICI resistance and improving cSCC patient outcomes.
283

284 **Materials and methods:**

285 <u>Animals</u>

286 All animal experiments were approved by the by the University of Utah Office of Comparative
287 Medicine (IACUC #22-02003) or by the University of California San Francisco Laboratory Animal
288 Resource Center (IACUC #AN187679). This work complies with all the relevant ethical
289 regulations regarding animal research. *K5CreER-Confetti FVB/N* mice were maintained in the
290 Reeves Lab colony at the University of California San Francisco. Eight-week-old wild-type FVB/N
291 mice were purchased from Jackson Laboratories. All experiments were performed on 8-16-
292 week old mice. Any diversity in mouse age or sex was addressed by distributing age and sex
293 cohorts evenly between different experimental arms.
294
295 Carcinogenesis and cell line generation
296 To induce tumors, *K5CreER-Confetti FVB/N* mice were treated with 25 µg DMBA followed by
297 TPA (200 µl of a 10^{-4} M solution in acetone) two times a week for 20 weeks. To generate cell
298 lines, carcinomas were resected at a size of >1 cm in longest diameter, finely chopped, digested
299 in DMEM containing Collagenase I and IV and DNase I for 45 minutes at 37 °C, washed with PBS,
300 plated in DMEM plus 10% heat-inactivated FBS and L-glutamine, with penicillin, streptomycin,
301 and amphotericin B, and passaged until cells stably grew in culture.
302
303 In vivo experiments and immune checkpoint inhibitor treatment
304 A total of 1.25×10^5 cells were injected subcutaneously into the dorsal flank of 8 to 16 week old
305 male and female FVB/N mice. For baseline flow cytometric immune profiling and histological
306 analysis (Fig. 1), tumors were harvested approximately 21 days post-engraftment, when tumors
307 measured ~1cm in diameter. For immune checkpoint inhibitor (ICI) experiments (Fig. 3), mice

308 were enrolled in treatment 14 days post-tumor engraftement, when tumors grew to 25-100
309 mm^3 in volume. Any mice with tumors <25 mm^3 or >100 mm^3 on the day(s) of enrollment were
310 excluded from the experiment. Mice were treated with 200 µg anti-PD-1 (BioXCell Catalog#
311 BE0146) and 200 µg anti-CTLA-4 (BioXCell Catalog# BE0131) or 200 µg isotype control (BioXCell
312 Catalog# BE0089). Mice received two doses 3 days apart. Mice were harvested when tumors
313 were ~10mm in length, typically 17-21 days post-ICI enrollment and 31-35 days post-tumor
314 engraftment, or when an ethical endpoint was reached.
315
316 Flow cytometric immune profiling
317 Harvested tumors were finely chopped, digested in DMEM containing Collagenase IV (Sigma-
318 Aldrich Catalog# 9001-12-1) and DNase I (Sigma-Aldrich Catalog# D5025-15KU) for 45 minutes
319 at 37 °C, and filtered through 70um filters. Cells were counted using a Countess III, and 5 million
320 cells were plated and stained with antibodies and Live/Dead NIR stain. Antibodies used for flow
321 cytometric analyses are listed in Supp. Table 3. Flow cytometry analysis was performed on a
322 Cytek Aurora.
323
324 Histology
325 Harvested tumors were fixed in formalin for 24 hours, placed in cassettes (VWR Catalog#
326 18000), submerged in 70% ethanol, and submitted to ARUP Laboratories Research Histology
327 Core Laboratory, where they were embedded in paraffin, cut into 4µm-thick slices, stained with
328 hematoxylin and eosin (H&E) and mounted on slides. The 4µm slides were then analyzed by a
329 board-certified pathologist, A.G.

330

331 Cell line sequencing and analysis

332 DNA was extracted from cultured cells from each cell line and from tails of the mice in which
333 each tumor originated using the Qiagen DNeasy Blood & Tissue DNA purification kit (Qiagen).
334 Whole exome sequencing was performed using the Agilent Sure Select Mouse Exon capture kit,
335 and sequenced to an average depth of 153X on an Illumina HiSeq X by MedGenome, Inc. in
336 Redwood City, CA. Reads were trimmed with cutadapt (v3.5)[33] and aligned to the mm10 mouse
337 genome using BWA (v0.7.17)[34]. Reads were deduplicated using MarkDuplicates and
338 recalibrated using BaseRecalibrator from GATK (v4.1)[35]. Mutations were called using MuTect2
339 (GATK v4.1)[35,36] and Strelka2 (v2.9.10)[37], using tails from the mice in which each tumor
340 developed as the matched normal. Mutation calls were filtered using the following criteria:
341 minimum read depth of 10 at the mutation position in both tumor and normal samples;
342 minimum of 4 reads supporting the mutation call; for Strelka only, minimum quality QSS score
343 of 25. Mutations that passed all filters with both callers were kept and were additionally filtered
344 to remove any germline SNP detected in the panel of normals. Final mutation calls were
345 annotated with Annovar[38]. Copy number calling was performed with CNVkit (v0.9.10)[39], using
346 all tails as a pooled normal. *Cdkn2a* deletions were confirmed by samtools (v1.16)[40] mpileups of
347 all reads aligning to the *Cdkn2a* locus (chr4:89,274,541-89,294,653). Exome sequencing data
348 from CIT lines is available in SRA (accession number PRJNA1129114).

349

350 Neoantigen peptide prediction

351 Mutations identified by exome sequencing were used to construct wild-type and mutant amino
352 acid sequences of all 7mer, 8mer, and 9mer peptides that included each identified single
353 nucleotide variant. The NetH2pan algorithm was used to predict binding affinity and percentile
354 rank for each wild-type and mutant peptide sequence. This data was filtered using the following
355 criteria: mutant peptide with a percentile rank <0.5, log affinity ratio >0 (affinity ratio defined as
356 ratio of predicted binding affinity of mutant sequence dividesd by wild-type sequence), and a
357 gene expression >300 RPM based on RNAseq of whole CIT6 and CIT9 tumors.
358
359 ELISpot assays
360 Whole spleens were harvested from FVB mice and processed by crushing through a 70µm mesh
361 filter, pre-wet with 1X PBS, using a syringe plunger and washed. Red blood cells were lysed for 5
362 minutes using ACK lysis buffer and splenocytes counted. Spleens from CIT6-bearing FVB mice
363 were harvested 2-4 weeks after tumor inoculation. CD8+ T cells were isolated from whole
364 spleens using EasySep™ Mouse CD8+ T Cell Isolation Kits (STEMCELL Technologies Catalog#
365 19853) and CD4+ T cells were isolated from whole spleens using EasySep™ Mouse CD4+ T Cell
366 Isolation (STEMCELL Technologies Catalog# 19852).
367 Interferon-gamma (IFNγ) ELISpots were performed over a three-day assay.
368 Multiscreen®HTS 96-well filtration plate(s) were coated with IFNγ capture antibody (clone AN-
369 18, Catalog# 517902), diluted 1:500 in 1X PBS. Plates were wrapped in aluminum foil to equally
370 distribute temperature and incubated overnight, or at least 18 hours, at 4°C. The following day
371 plates were washed twice with 200µl RPMI-2 (RPMI with 2% FBS, 1% L-glutamate, 1%
372 streptococcus and penicillin antibiotic solution, and 0.09% 2-Mercaptoethanol (BME)) and

373 blocked for two hours with 200µl of RPMI-20 (RPMI with 20% FBS, 1% L-glutamate, 1%
374 streptococcus and penicillin antibiotic solution, and 0.09% 2-Mercaptoethanol (BME)) before
375 splenocytes or T cells were added. For assays where total splenocytes were used, 500,000
376 splenocytes were plated per well. For assays using CD8+ and CD4+ T cells, 20,000 cells per well
377 were co-cultured with 500,000 splenocytes from a non-tumor-bearing mouse to provide a
378 source of antigen presenting cells. Stimulation medium was prepared by diluting synthetic
379 peptide in RPMI-10 to desired peptide concentration(s). All synthetic peptides used for these
380 assays were ordered through GenScript. Peptides were reconstituted in DMSO or MilliQ water
381 according to solubility testing provided by the manufacturer. Reconstituted peptides were
382 aliquoted and frozen at -80°C. The negative control consisted of MilliQ water and RPMI-10.
383 Positive control contained 0.04% Phorbol 12-myristate 13-acetate (PMA) and 0.09% Ionomycin
384 in RPMI-10.
385 Plates were wrapped in aluminum foil and incubated undisturbed at 37°C and 5% CO2
386 for 44-48 hours before developing using biotinylated anti-IFNγ detection antibody (clone R4-
387 6A2, Catalog# 505704), streptavidin-HRP enzyme conjugation (Thermofisher, Catalog# 405210),
388 and AEC (3-amino-9-ethyl-carbazole) substrate. AEC substrate was prepared by dissolving 20
389 mg of AEC in 2 ml of N, N Dimethylforamamide (Sigma-Aldrich, Catalog# 227056), diluting in 0.1
390 M Acetate Solution, adding hydrogen peroxide and filtering with a 0.45µM filter. Spots were
391 Imaged using the Agilent BioTek Cytation7 and analyzed using the Gen5 software.
392
393 Statistical analysis

394 To determine significant statistical differences, Welch's t-test was used when comparing 2
395 groups, and one-way ANOVA with Tukey post-hoc test was uses when comparing 3 or more
396 groups. Paired analyses were performed by paired t-test. Hypothesis testing was performed
397 using R open-source software (v4.4.2) and Prism software (GraphPad v10.4.2). Significant *p*
398 values are marked as * $p < 0.05$, ** $p < 0.01$, *** $p < 0.001$, **** $p < 0.0001$. Studies were not
399 blinded. Power calculations to determine appropriate cohort size were performed using
400 Sample-Size software available online.
401
402 **Data availability**
403 Exome sequencing of CIT lines is available in SRA (accession number PRJNA1129114).
404
405 **Acknowledgements**
406 This work was supported by the UCSF Program for Breakthrough Biomedical Research (PBBR)
407 Sandler Fellowship, US National Cancer Institute (NCI) grant R21CA264599, the Huntsman
408 Cancer Institute Cancer Center Support Grant P30CA040214, the American Cancer Society IRG-
409 21-131-01, Five For The Fight, The Cancer League, and the V Foundation (V2024-002). G.S. is
410 supported by the Institute of General Medical Sciences grant T32GM141848. The
411 computational resources used for exome sequencing analysis were partially funded by the NIH
412 Shared Instrumentation Grant 1S10OD021644-01A1. We thank the University of Utah Flow
413 Cytometry Core; the Associated Regional and University Pathologists, Inc. (ARUP Laboratories)
414 Research Histology Core; the University of Utah Center for High Performance Computing
415 (CHPC); the Huntsman Cancer Institute Precision Cancer Models (PCM) Shared Resource

416 (supported by P30CA042014), in particular D. Lum and W. Sun; the Immune Oncology Network
417 (ION), in particular E. Cortes-Sanchez; and the UCSF Parnassus Flow CoLab. We also thank A. Lai
418 for help establishing the ELISPOT methods. We thank and all members of the Reeves Lab for
419 thoughtful input during the development of this story. Some figures were created with
420 Biorender.com.

421

422 **Author contributions**

423 M.T., R.L., L.L., A.B., and M.Q.R. designed the project and experiments. R.L., S.H., M.T., L.L. and
424 M.Q.R. led experiment implementation and data analysis. A.B. designed and carried out the
425 neoantigen identification experiments. S.H. and G.S. carried out the immune checkpoint
426 inhibitor experiments, with support from R.L. Board-certified pathologist A.G. provided
427 histology review. R.L., M.T., D.C.D., and M.Q.R. wrote the manuscript, with input from other co-
428 authors. P.C., K.N., D.S., C.M.L. and M.G. assisted with experiments.

429

430 **References**

431 1. Karia, P. S., Han, J. & Schmults, C. D. Cutaneous squamous cell carcinoma: Estimated
432 incidence of disease, nodal metastasis, and deaths from disease in the United States, 2012.
433 *J. Am. Acad. Dermatol.* **68**, 957–966 (2013).
434 2. Rogers, H. W., Weinstock, M. A., Feldman, S. R. & Coldiron, B. M. Incidence Estimate of
435 Nonmelanoma Skin Cancer (Keratinocyte Carcinomas) in the US Population, 2012. *JAMA*
436 *Dermatol.* **151**, 1081 (2015).

437 3. Nehal, K. S. & Bichakjian, C. K. Update on Keratinocyte Carcinomas. *N. Engl. J. Med.* **379**,
438 363–374 (2018).
439 4. Mansouri, B. & Housewright, C. D. The Treatment of Actinic Keratoses—The Rule Rather
440 Than the Exception. *JAMA Dermatol.* **153**, 1200 (2017).
441 5. Mourouzis, C. *et al.* Cutaneous head and neck SCCs and risk of nodal metastasis – UK
442 experience. *J. Cranio-Maxillofac. Surg.* **37**, 443–447 (2009).
443 6. Brantsch, K. D. *et al.* Analysis of risk factors determining prognosis of cutaneous squamous-
444 cell carcinoma: a prospective study. *Lancet Oncol.* **9**, 713–720 (2008).
445 7. Ribas, A. & Wolchok, J. D. Cancer immunotherapy using checkpoint blockade. *Science* **359**,
446 1350–1355 (2018).
447 8. Chen, D. S. & Mellman, I. Elements of cancer immunity and the cancer–immune set point.
448 *Nature* **541**, 321–330 (2017).
449 9. Ansary, T. M., Hossain, M. R., Komine, M. & Ohtsuki, M. Immunotherapy for the Treatment
450 of Squamous Cell Carcinoma: Potential Benefits and Challenges. *Int. J. Mol. Sci.* **23**, 8530
451 (2022).
452 10. Gross, N. D. *et al.* Neoadjuvant Cemiplimab for Stage II to IV Cutaneous Squamous-Cell
453 Carcinoma. *N. Engl. J. Med.* **387**, 1557–1568 (2022).
454 11. Hughes, B. G. M. *et al.* Pembrolizumab for locally advanced and recurrent/metastatic
455 cutaneous squamous cell carcinoma (KEYNOTE-629 study): an open-label, nonrandomized,
456 multicenter, phase II trial. *Ann. Oncol.* **32**, 1276–1285 (2021).
457 12. Migden, M. R. *et al.* PD-1 Blockade with Cemiplimab in Advanced Cutaneous Squamous-Cell
458 Carcinoma. *N. Engl. J. Med.* **379**, 341–351 (2018).

459 13. Grob, J.-J. *et al.* Pembrolizumab Monotherapy for Recurrent or Metastatic Cutaneous
460 Squamous Cell Carcinoma: A Single-Arm Phase II Trial (KEYNOTE-629). *J. Clin. Oncol.* **38**,
461 2916–2925 (2020).
462 14. Chang, D. & Shain, A. H. The landscape of driver mutations in cutaneous squamous cell
463 carcinoma. *Npj Genomic Med.* **6**, 61 (2021).
464 15. Pickering, C. R. *et al.* Mutational Landscape of Aggressive Cutaneous Squamous Cell
465 Carcinoma. *Clin. Cancer Res.* **20**, 6582–6592 (2014).
466 16. Gubin, M. M. *et al.* Checkpoint blockade cancer immunotherapy targets tumour-specific
467 mutant antigens. *Nature* **515**, 577–581 (2014).
468 17. McCreery, M. Q. *et al.* Evolution of metastasis revealed by mutational landscapes of
469 chemically induced skin cancers. *Nat. Med.* **21**, 1514–1520 (2015).
470 18. Wong, C. E. *et al.* Inflammation and Hras signaling control epithelial–mesenchymal
471 transition during skin tumor progression. *Genes Dev.* **27**, 670–682 (2013).
472 19. Li, Y. R. *et al.* Long-Term Latency of Highly Mutated Cells in Normal Mouse Skin Is Reversed
473 by Exposure to Tumor Promoters and Chronic Tissue Damage. *Cancer Discov.* **15**, 1115–
474 1128 (2025).
475 20. Nassar, D., Latil, M., Boeckx, B., Lambrechts, D. & Blanpain, C. Genomic landscape of
476 carcinogen-induced and genetically induced mouse skin squamous cell carcinoma. *Nat.*
477 *Med.* **21**, 946–954 (2015).
478 21. DeVette, C. I. *et al.* NetH2pan: A Computational Tool to Guide MHC Peptide Prediction on
479 Murine Tumors. *Cancer Immunol. Res.* **6**, 636–644 (2018).

480 22. Castle, J. C. *et al.* Exploiting the Mutanome for Tumor Vaccination. *Cancer Res.* **72**, 1081–
481 1091 (2012).
482 23. Alspach, E. *et al.* MHC-II neoantigens shape tumour immunity and response to
483 immunotherapy. *Nature* **574**, 696–701 (2019).
484 24. Matsushita, H. *et al.* Cancer exome analysis reveals a T-cell-dependent mechanism of
485 cancer immunoediting. *Nature* **482**, 400–404 (2012).
486 25. Yadav, M. *et al.* Predicting immunogenic tumour mutations by combining mass
487 spectrometry and exome sequencing. *Nature* **515**, 572–576 (2014).
488 26. Roerden, M. *et al.* Neoantigen architectures define immunogenicity and drive immune
489 evasion of tumors with heterogenous neoantigen expression. *J. Immunother. Cancer* **12**,
490 e010249 (2024).
491 27. Sellers, R. S., Clifford, C. B., Treuting, P. M. & Brayton, C. Immunological Variation Between
492 Inbred Laboratory Mouse Strains: Points to Consider in Phenotyping Genetically
493 Immunomodified Mice. *Vet. Pathol.* **49**, 32–43 (2012).
494 28. Davie, S. A. *et al.* Effects of FVB/NJ and C57Bl/6J strain backgrounds on mammary tumor
495 phenotype in inducible nitric oxide synthase deficient mice. *Transgenic Res.* **16**, 193–201
496 (2007).
497 29. Hennings, H., Shores, R., Mitchell, P., Spangler, E. F. & Yuspa, S. H. Induction of papillomas
498 with a high probability of conversion to malignancy. *Carcinogenesis* **6**, 1607–1610 (1985).
499 30. Kim, E.-M., Bae, Y. M., Choi, M.-H. & Hong, S.-T. Cyst formation, increased anti-
500 inflammatory cytokines and expression of chemokines support for Clonorchis sinensis
501 infection in FVB mice. *Parasitol. Int.* **61**, 124–129 (2012).

502 31. Reeves, M. Q., Kandyba, E., Harris, S., Del Rosario, R. & Balmain, A. Multicolour lineage
503 tracing reveals clonal dynamics of squamous carcinoma evolution from initiation to
504 metastasis. *Nat. Cell Biol.* **20**, 699–709 (2018).
505 32. Tanaka, M. *et al.* Tumor cell heterogeneity drives spatial organization of the intratumoral
506 immune response. *J. Exp. Med.* **222**, e20242282 (2025).
507 33. Martin, M. Cutadapt removes adapter sequences from high-throughput sequencing reads.
508 *EMBnet.journal* **17**, 10 (2011).
509 34. Li, H. & Durbin, R. Fast and accurate short read alignment with Burrows–Wheeler
510 transform. *Bioinformatics* **25**, 1754–1760 (2009).
511 35. Van der Auwera, G. A. & O'Connor, B. D. *Genomics in the Cloud: Using Docker, GATK, and*
512 *WDL in Terra*. (O'Reilly Media, 2020).
513 36. Cibulskis, K. *et al.* Sensitive detection of somatic point mutations in impure and
514 heterogeneous cancer samples. *Nat. Biotechnol.* **31**, 213–219 (2013).
515 37. Kim, S. *et al.* Strelka2: fast and accurate calling of germline and somatic variants. *Nat.*
516 *Methods* **15**, 591–594 (2018).
517 38. Wang, K., Li, M. & Hakonarson, H. ANNOVAR: functional annotation of genetic variants from
518 high-throughput sequencing data. *Nucleic Acids Res.* **38**, e164–e164 (2010).
519 39. Talevich, E., Shain, A. H., Botton, T. & Bastian, B. C. CNVkit: Genome-Wide Copy Number
520 Detection and Visualization from Targeted DNA Sequencing. *PLOS Comput. Biol.* **12**,
521 e1004873 (2016).

522 40. Li, H. A statistical framework for SNP calling, mutation discovery, association mapping and
523 population genetical parameter estimation from sequencing data. *Bioinformatics* **27**, 2987–
524 2993 (2011).
525

Figure 1

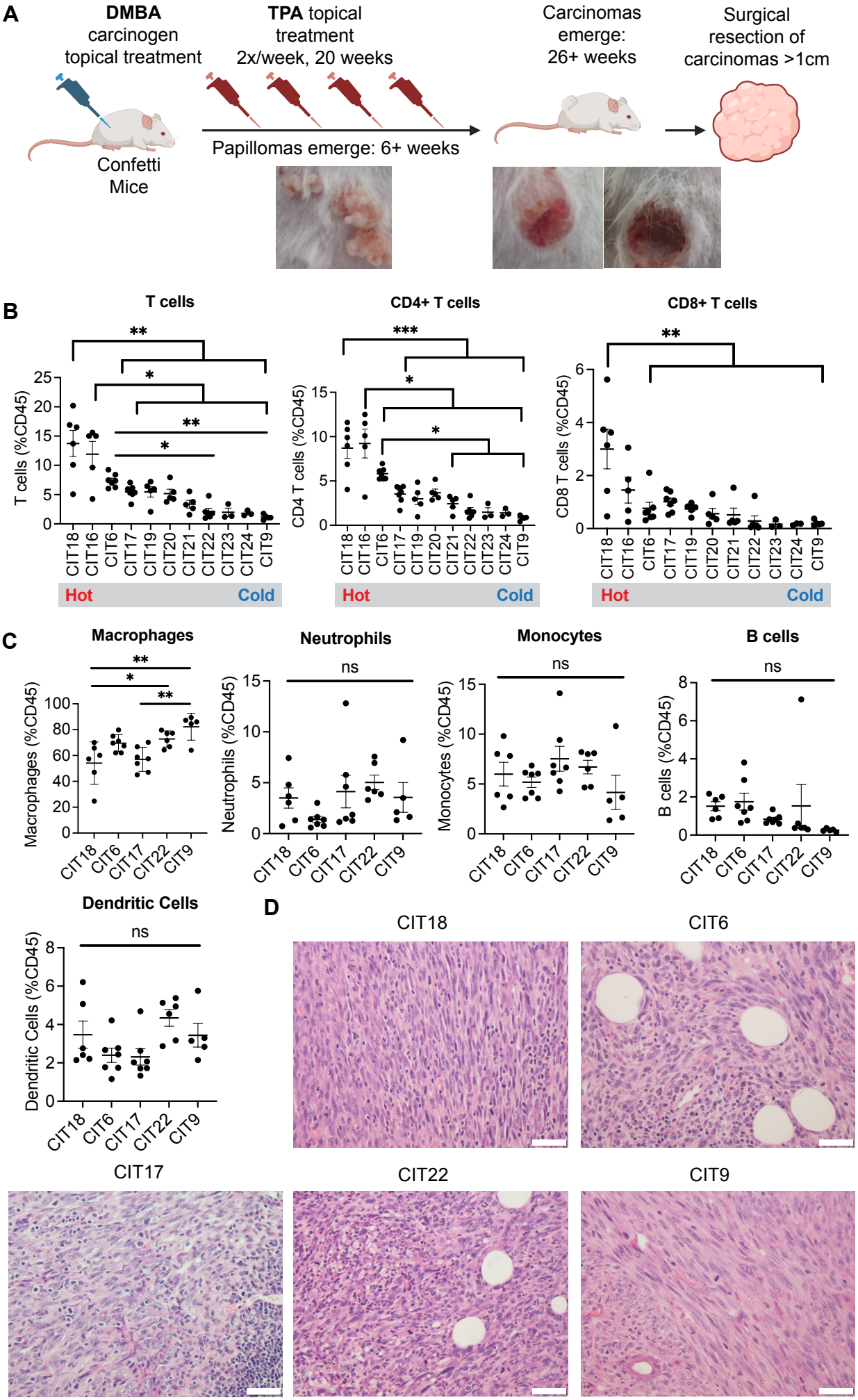
A
DMBA carcinogen topical treatment
Confetti Mice
TPA topical treatment 2x/week, 20 weeks
Papillomas emerge: 6+ weeks
Carcinomas emerge: 26+ weeks
Surgical resection of carcinomas >1cm
B
T cells
CD4+ T cells
CD8+ T cells
T cells (%CD45)
CD4 T cells (%CD45)
CD8 T cells (%CD45)
CIT18 CIT16 CIT6 CIT17 CIT19 CIT20 CIT21 CIT22 CIT23 CIT24 CIT9
Hot
Cold
C
Macrophages
Neutrophils
Monocytes
B cells
Dendritic Cells
Macrophages (%CD45)
Neutrophils (%CD45)
Monocytes (%CD45)
B cells (%CD45)
Dendritic Cells (%CD45)
ns
CIT18 CIT6 CIT17 CIT22 CIT9
D
CIT18
CIT6
CIT17
CIT22
CIT9

526 **Figure 1. Immune infiltration and histology profiles of CIT lines.**

527 **(A)** Schematic of CIT cell line generation. Tumors were induced with the DMBA/TPA

528 carcinogenesis model, and cell lines were established from malignant carcinomas. **(B)**

529 Quantification of total T cells, CD4+ T cells and CD8+ T cells by flow cytometry in each CIT line.

530 (n=5-7 mice per group; * $p < 0.05$, ** $p < 0.01$, *** $p < 0.001$) **(C)** Quantification of

531 macrophages, neutrophils, monocytes, B cells and dendritic cells by flow cytometry in 5

532 selected CIT lines. (n=5-7 mice per group; * $p < 0.05$, ** $p < 0.01$, ns = not significant) **(D)**

533 Representative images of tumors from selected CIT lines stained with hematoxylin and eosin

534 (H&E) for histological analysis. Scale bar = 20 μm. Statistical analysis in (B-C) by one-way ANOVA

535 with Tukey post-hoc test.

536

537

Figure 2

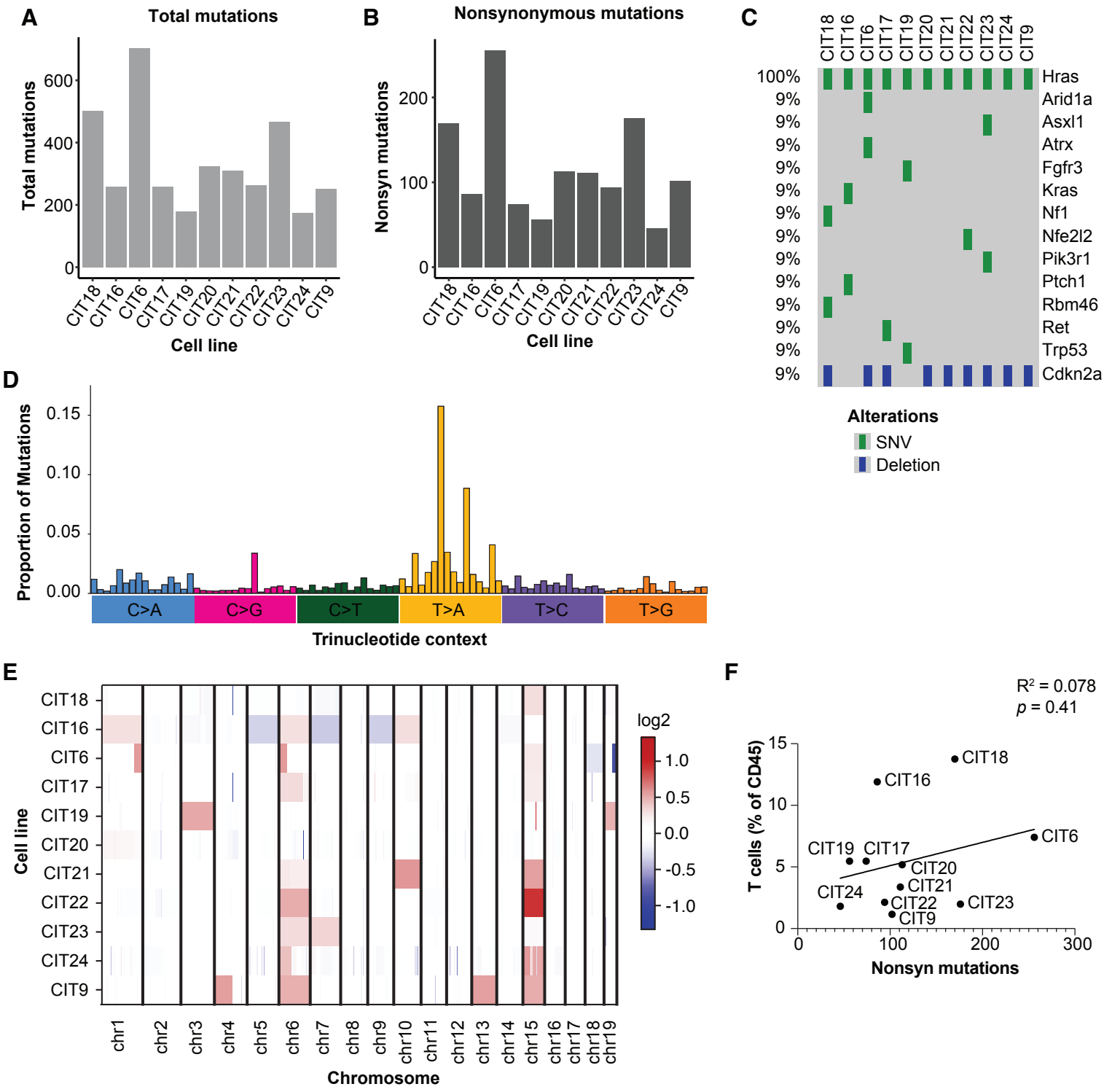
A
Total mutations
Total mutations
0
200
400
600
CIT18
CIT16
CIT6
CIT17
CIT19
CIT20
CIT21
CIT22
CIT23
CIT24
CIT9
Cell line
B
Nonsynonymous mutations
Nonsyn mutations
0
100
200
Cell line
C
100% Hras
9% Arid1a
9% Asxl1
9% Atrx
9% Fgfr3
9% Kras
9% Nf1
9% Nfe2l2
9% Pik3r1
9% Ptch1
9% Rbm46
9% Ret
9% Trp53
9% Cdkn2a
Alterations
SNV
Deletion
D
Proportion of Mutations
0.00
0.05
0.10
0.15
C>A
C>G
C>T
T>A
T>C
T>G
Trinucleotide context
E
Cell line
log2
1.0
0.5
0.0
-0.5
-1.0
chr1
chr2
chr3
chr4
chr5
chr6
chr7
chr8
chr9
chr10
chr11
chr12
chr13
chr14
chr15
chr16
chr17
chr18
chr19
Chromosome
F
R² = 0.078
p = 0.41
T cells (% of CD45)
Nonsyn mutations
0
5
10
15
100
200
300
CIT18
CIT16
CIT6
CIT19
CIT17
CIT20
CIT21
CIT24
CIT22
CIT23
CIT9

538 **Figure 2. Genetic profiling of CIT lines.**

539 **(A-B)** Number of total (A) and non-synonymous (B) mutations per cell line, based on exome
540 sequencing. **(C)** Genes mutated in CIT lines which are known to be commonly mutated in
541 human SCC, and CIT lines with *Cdkn2a* deletions. **(D)** Frequencies of mutations observed in each
542 of 96 possible trinucleotide contexts for all mutations in CIT cell lines. Trinucleotide contexts,
543 arranged on the x axis, are grouped by the base pair change of the mutation. Highest peaks are
544 observed at CTG>A and GTG>A. **(E)** CNV alterations detected in each chromosome in CIT lines
545 based on exome sequencing. Red denotes copy number gains, blue denotes copy number
546 losses. **(F)** Scatter plot showing relationship between non-synonymous mutations (based on
547 exome sequencing) and T cell infiltrate (based on flow cytometry) for CIT lines. There is no
548 significant correlation between these metrics.

549

Figure 3

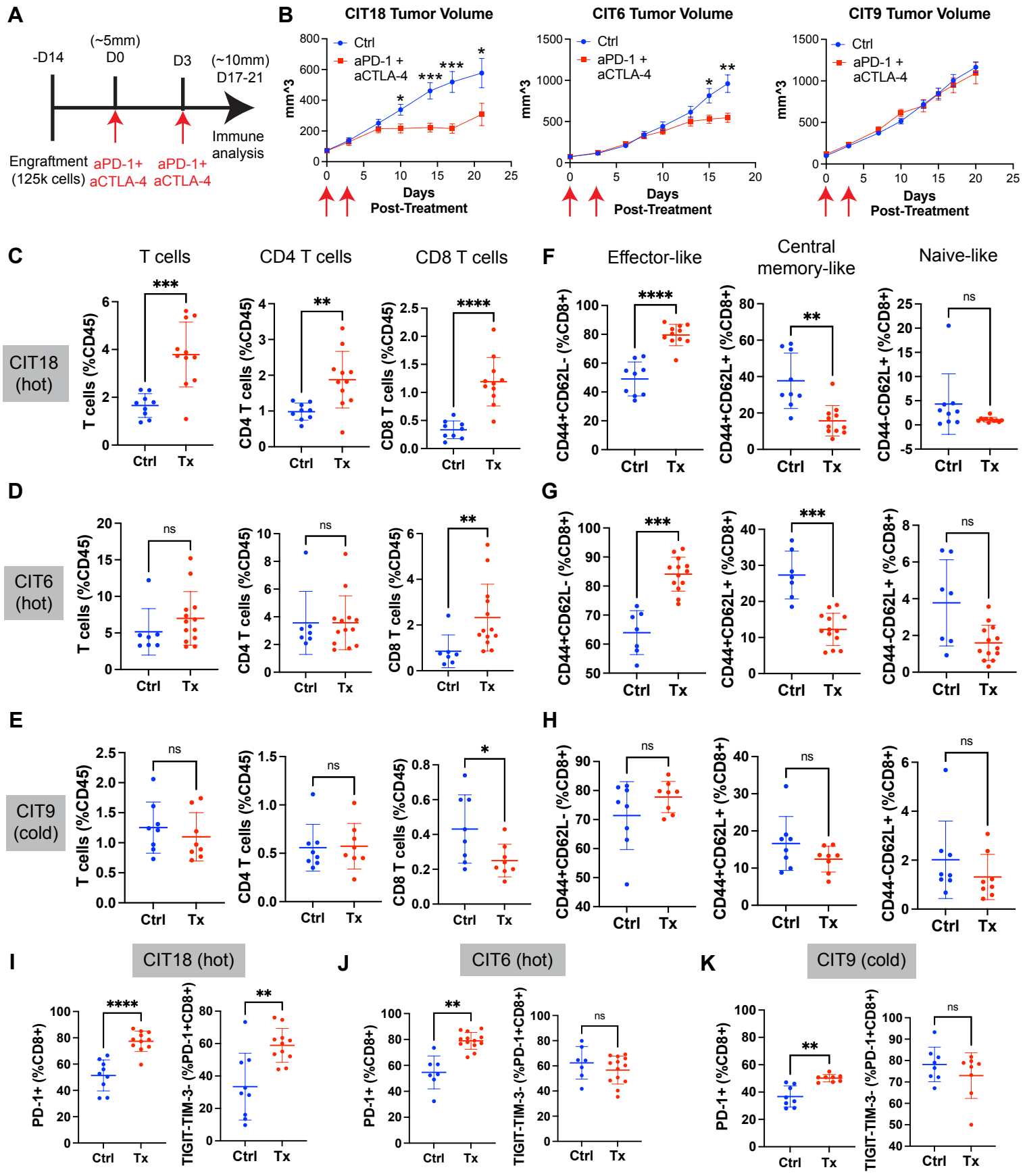
A
-D14
(~5mm)
D0
D3
(~10mm)
D17-21
Immune analysis
Engraftment (125k cells)
aPD-1+ aCTLA-4
aPD-1+ aCTLA-4
B
CIT18 Tumor Volume
CIT6 Tumor Volume
CIT9 Tumor Volume
Ctrl
aPD-1 + aCTLA-4
mm^3
Days Post-Treatment
C
T cells
CD4 T cells
CD8 T cells
CIT18 (hot)
T cells (%CD45)
CD4 T cells (%CD45)
CD8 T cells (%CD45)
Ctrl
Tx
D
CIT6 (hot)
E
CIT9 (cold)
F
Effector-like
Central memory-like
Naive-like
CD44+CD62L- (%CD8+)
CD44+CD62L+ (%CD8+)
CD44-CD62L+ (%CD8+)
G
H
ns
I
CIT18 (hot)
PD-1+ (%CD8+)
TIGIT-TIM-3- (%PD-1+CD8+)
J
CIT6 (hot)
K
CIT9 (cold)

550 **Figure 3. Immunologically hot CIT lines are responsive to combined anti-PD-1 and anti-CTLA-4**
551 **immune checkpoint inhibitor (ICI) therapy.**
552 **(A)** Schematic of ICI treatment regimen on CIT tumor-bearing mice. **(B)** Average tumor volumes
553 of immunologically hot CIT18 and CIT6 tumors and immunologically cold CIT9 tumors after
554 combined ICI therapy, compared to tumors treated with isotype control antibodies. Error bars
555 represent mean and standard error. **(C-E)** Total T cell, CD4+ T cell, and CD8+ T cell infiltration of
556 CIT18 (C), CIT6 (D) and CIT9 (E) tumors as a percentage of all CD45+ immune cells for control-
557 treated ("Ctrl") or ICI-treated ("Tx") tumors. **(F-H)** Abundance of effector subsets of CD8+ T cells
558 defined by the combinatorial expressions of CD44 and CD62L in CIT18 (F), CIT6 (G) and CIT9 (H)
559 tumors. **(I-K)** Abundance of CD8+ T cells expressing PD-1, and frequency of "activated" PD-
560 1+Tim3-TIGIT- CD8+ T cells in CIT18 (I), CIT6 (J) and CIT9 (K) tumors. All statistical analyses
561 performed with Welch's t-test, n=7-13 mice per group. * $p < 0.05$, ** $p < 0.01$, *** $p < 0.001$,
562 **** $p < 0.0001$.
563
564

Figure 4

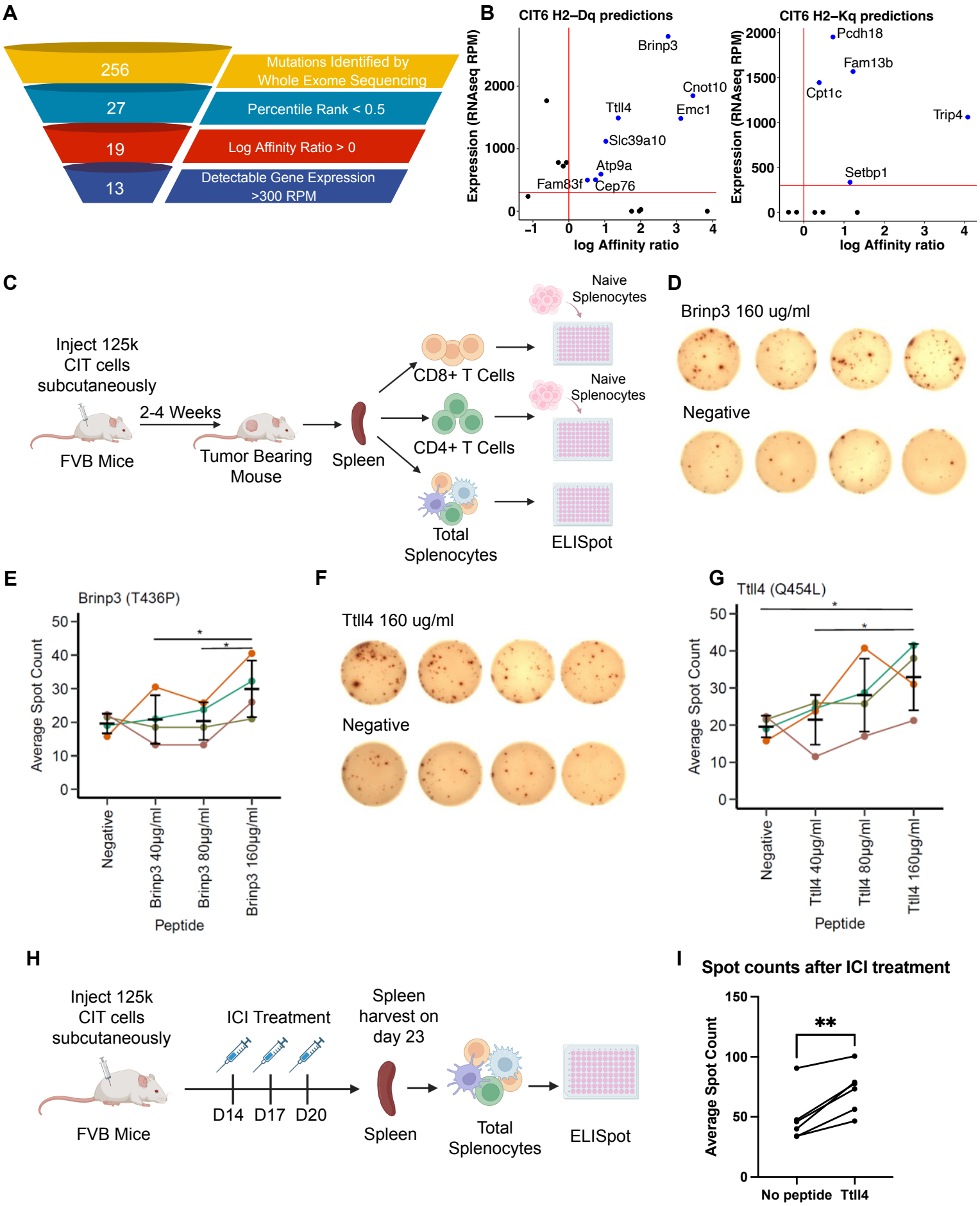
A
256
Mutations Identified by Whole Exome Sequencing
27
Percentile Rank < 0.5
19
Log Affinity Ratio > 0
13
Detectable Gene Expression >300 RPM
B
CIT6 H2–Dq predictions
Expression (RNAseq RPM)
log Affinity ratio
Brinp3
Cnot10
Ttll4
Emc1
Slc39a10
Atp9a
Fam83f
Cep76
CIT6 H2–Kq predictions
Pcdh18
Fam13b
Cpt1c
Trip4
Setbp1
C
Inject 125k CIT cells subcutaneously
FVB Mice
2-4 Weeks
Tumor Bearing Mouse
Spleen
CD8+ T Cells
CD4+ T Cells
Total Splenocytes
Naive Splenocytes
ELISpot
D
Brinp3 160 ug/ml
Negative
E
Brinp3 (T436P)
Average Spot Count
Negative
Brinp3 40µg/ml
Brinp3 80µg/ml
Brinp3 160µg/ml
Peptide
F
Ttll4 160 ug/ml
Negative
G
Ttll4 (Q454L)
Average Spot Count
Negative
Ttll4 40µg/ml
Ttll4 80µg/ml
Ttll4 160µg/ml
Peptide
H
Inject 125k CIT cells subcutaneously
FVB Mice
ICI Treatment
D14 D17 D20
Spleen harvest on day 23
Spleen
Total Splenocytes
ELISpot
I
Spot counts after ICI treatment
Average Spot Count
No peptide
Ttll4

565 **Figure 4. CIT lines express identifiable neoantigens whose cognate CD8+ T cells are responsive**
566 **to immunotherapy.**
567 **(A)** Selection criteria for CIT6 mutations predicted to generate neoantigens. **(B)** Predicted
568 peptide log affinity ratio (affinity ratio is defined as ratio between predicted binding affinity of
569 mutant versus wild-type sequence) and gene expression level of mutations predicted to be top
570 CIT6 candidate neoantigens, shown for H2-Dq and H2-Kq alleles. Affinity predictions were
571 generated using NetH2Pan algorithm. **(C)** Schematic of IFNγ ELISpot assay. For screening of
572 CD8+ T cell and CD4+ T cell responses, CD8+ or CD4+ T cells were isolated from the spleens of
573 tumor bearing mice and co-cultured with total splenoyctes from a healthy tumor-naïve mouse.
574 **(D)** Representative IFNγ ELISpot images of assay peformed with CD8+ T cells from the spleen of
575 CIT6-bearing mice cultured with 160ug/ml of Brinp3 peptide CPAFLPCTV (top row) and negative
576 control (no peptide, bottom row). **(E)** Quantification of average IFNγ ELISpot spot counts for
577 CD8+ T cells from the spleen of CIT6-bearing mice cultured with different concentrations of
578 Brinp3 peptide CPAFLPCTV. Each colored line represents data points from a different mouse
579 (n=4 mice). **(F)** Representative IFNγ ELISpot images of assay peformed with CD8+ T cells from
580 the spleen of CIT6-bearing mice cultured with 160ug/ml of Ttll4 peptide VPPSSLLPL (top row)
581 and negative control (no peptide, bottom row). **(G)** Quantification of average IFNγ ELISpot spot
582 counts for CD8+ T cells from the spleen of CIT6-bearing mice cultured with different
583 concentrations of Ttll4 peptide VPPSSLLPL. Each colored line represents data points from a
584 different mouse (n=4 mice). **(H)** Schematic of immune checkpoint inhibitor (ICI) treatment
585 regimen and ELISpot analysis. **(I)** Average spot counts of ICI-treated splenocytes cultured with
586 80ug/ml of Ttll4 peptide vs negative control. Each line represents data points from a different

587 mouse (n=6 mice). Statistical analysis in panels E, G, and I was done by paired t-test. * $p < 0.05$,

588 ** $p < 0.01$. Error bars in panels E and G represent mean and standard deviation.

Supplemental Figure 1

A

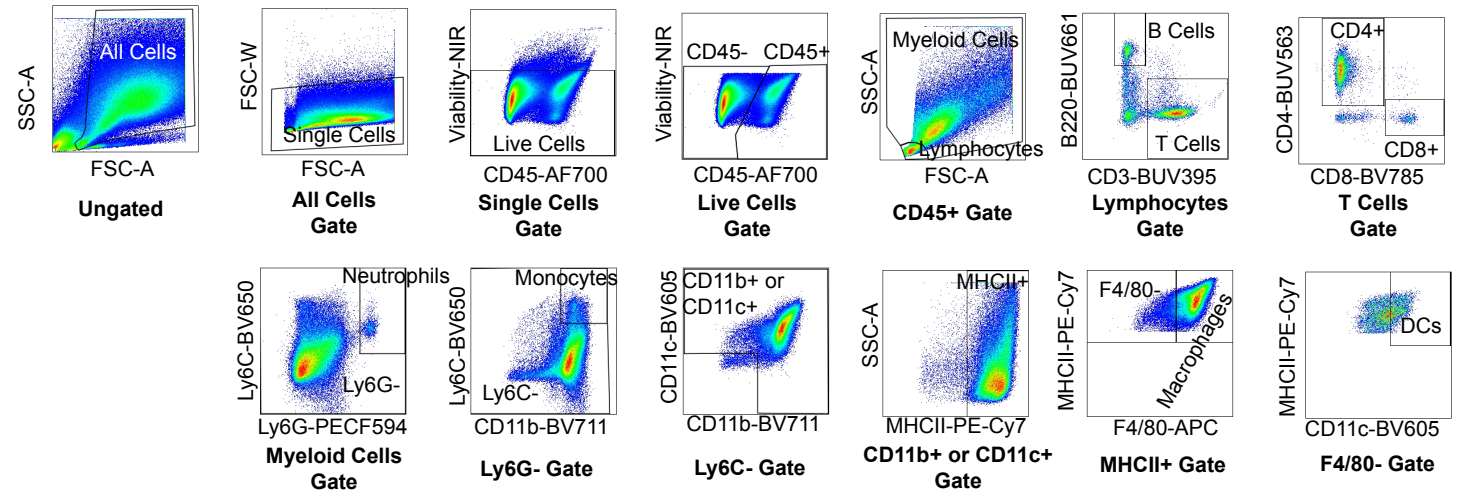

B

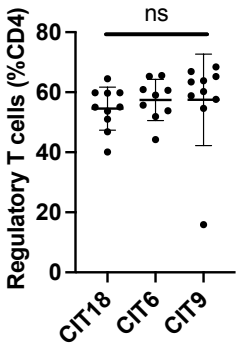

589 **Supp. Fig 1. Flow cytometry gating strategy and regulatory T cell infiltration in CIT tumors.**

590 **(A**) Flow cytometric gating strategy of main immune cell types. Immune analysis of a CIT6

591 tumor is shown as representative data. **(B)** Abundance of Foxp3+CD25+ regulatory T cells

592 (Tregs) as percentage of CD4+ T cells in CIT18, CIT6 and CIT9 tumors (n=9-10 mice per group).

593 Statistical analysis by One-way ANOVA with Tukey post-hoc test.

594

595

Supplemental Figure 2

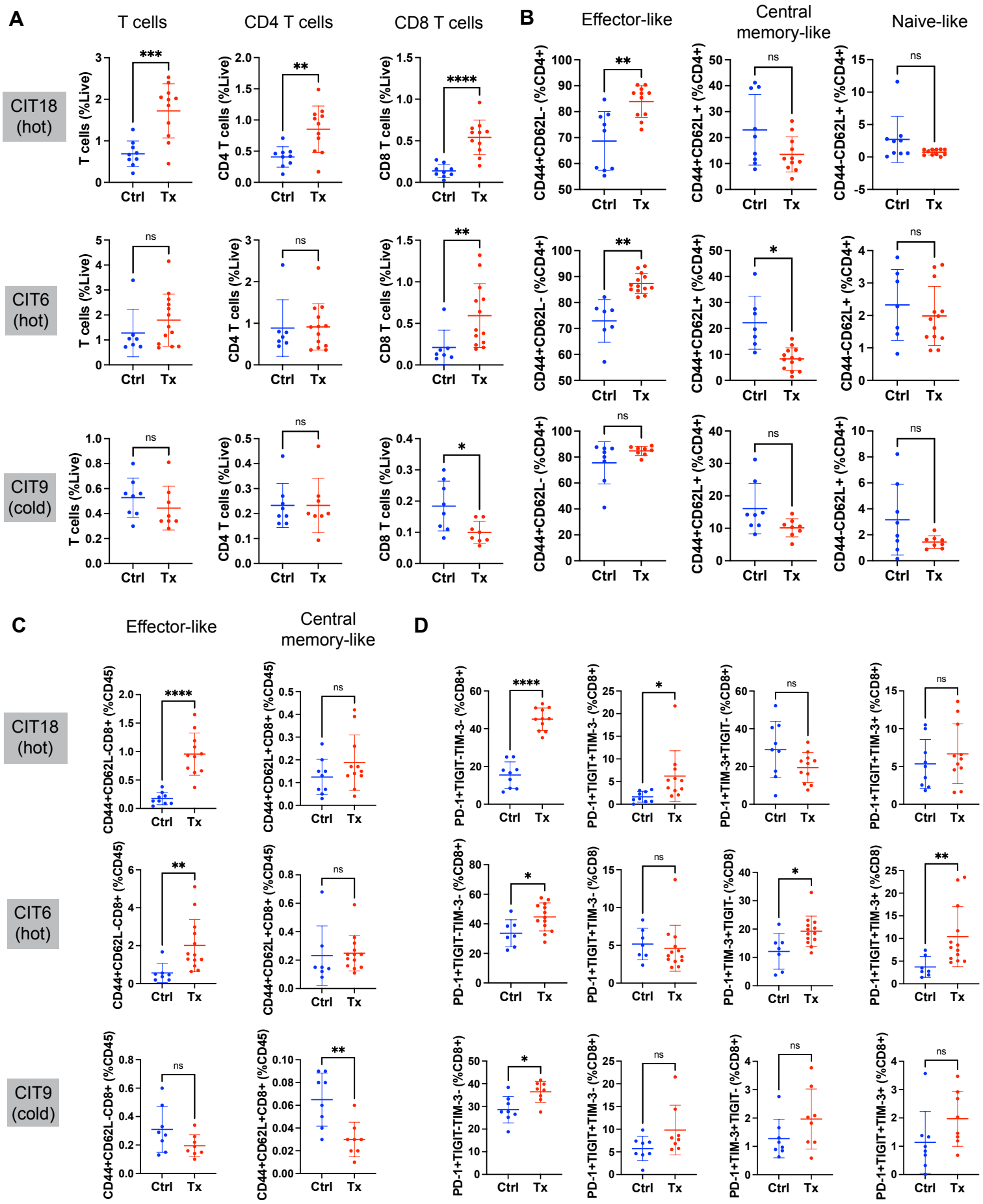

596 **Supp. Fig. 2. Tumor-infiltrating T cell effector activity after treatment with combined anti-PD-**

597 **1 and anti-CTLA-4 immune checkpoint inhibitor (ICI) therapy.**

598 **(A)** Total T cell, CD4+ T cell, and CD8+ T cell infiltration of CIT18, CIT6 and CIT9 as percentage of

599 all live cells, including tumor and stromal cells, for control-treated ("Ctrl") or ICI-treated ("Tx")

600 tumors. **(B)** Abundance of effector subsets of CD4+ T cells defined by the combinatorial

601 expressions of CD44 and CD62L in CIT18, CIT6 and CIT9. **(C)** Infiltration of CD44+CD62L-

602 "effector-like" CD8+ T cells and CD44+CD62L+ "central memory-like" CD8+ T cells as percentage

603 of all CD45+ immune cells. **(D)** Abundance of CD8+ PD-1+ T cells expressing specific

604 combinations of TIGIT and Tim3 exhaustion markers in CIT18, CIT6 and CIT9 tumors. All

605 statistical analyses performed with Welch's t-test, n=7-13 mice per group. * $p < 0.05$, ** $p <$

606 0.01, *** $p < 0.001$, **** $p < 0.0001$.

607

608

Supplemental Figure 3

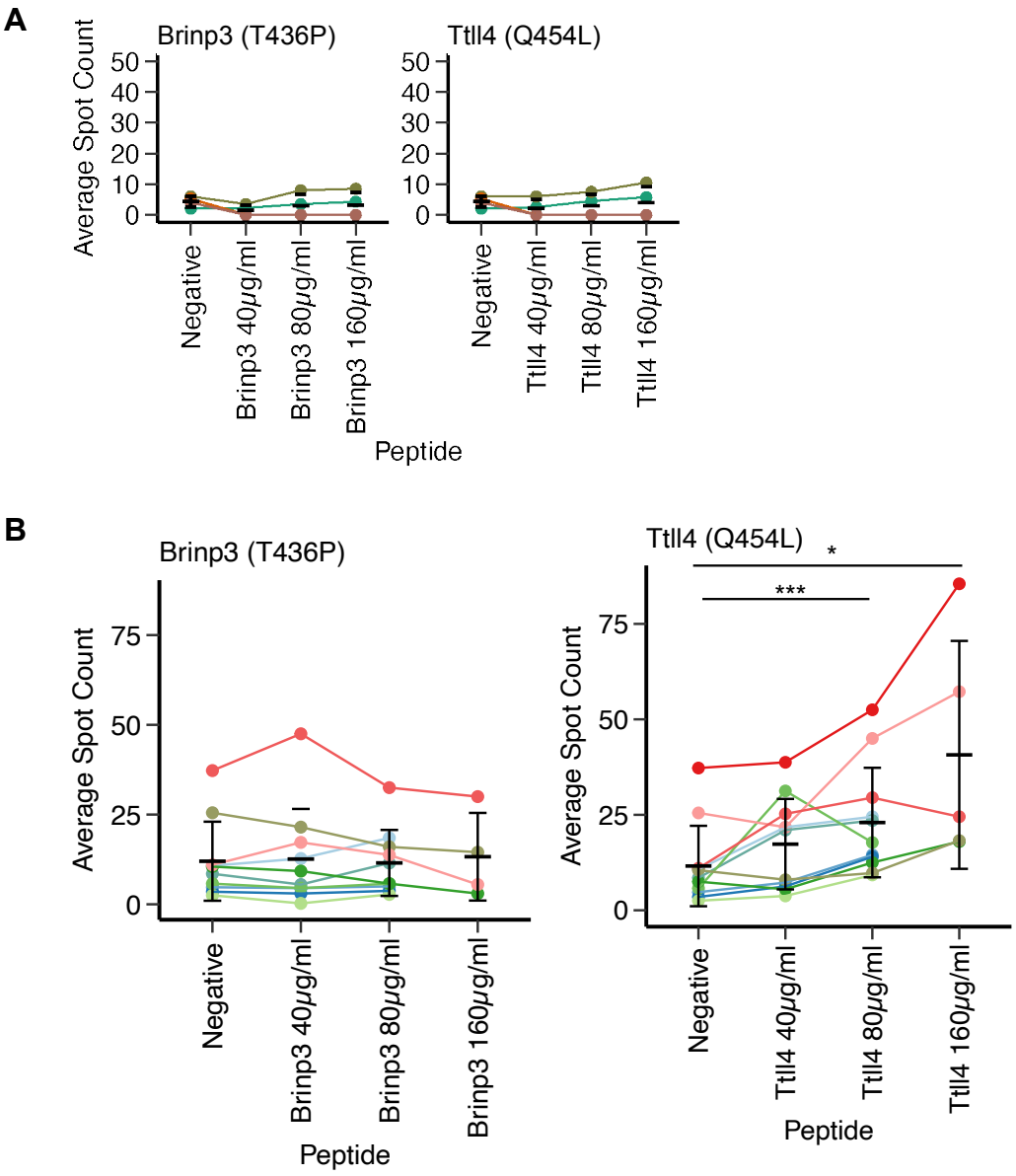

609 **Supp. Fig. 3. CIT6 ELISpot analysis of unfractionated splenocytes and CD4+ splenocytes.**

610 **(A)** Spot counts from ELISpot assays performed with CD4+ T cells isolated from the spleens of

611 CIT6-bearing mice and cultured with splenocytes from tumor-naïve mice loaded with increasing

612 concentrations of Brinp3 and Ttll4 peptides. Each colored line represents data points from a

613 different mouse (n=4 mice). **(B)** Spot counts from ELISpot assays performed with total

614 splenocytes from CIT6-bearing mice cultured with increasing concentrations of Brinp3 and Ttll4

615 peptides. Each colored line represents data points from a different mouse (n=10-11 mice). All

616 statistical analyses performed with paired t-test. * $p < 0.05$, *** $p < 0.001$. Error bars represent

617 mean and standard deviation.

618

619

Supp. Table 1: Mutations per CIT Cell Line			
Cell Line	**Total Mutations**	**Total Mutations per MB**	**Non-Synonymous Mutations**
CIT18	503	14.92	170
CIT16	259	7.76	86
CIT6	703	20.95	256
CIT17	258	7.74	74
CIT19	179	5.36	56
CIT20	324	9.66	113
CIT21	309	9.32	111
CIT22	264	7.91	94
CIT23	468	14.13	176
CIT24	174	5.22	46
CIT9	252	7.58	102

620 **Supp. Table 1: Number of total and non-synonymous mutations per CIT cell line.** Number of

621 total mutations, mutations per megabase, and non-synonymous mutations based on exome

622 sequencing of CIT cell lines.

623

624

Supp. Table 2: List of Filtered Peptide Candidates for CIT6 Antigens				
Gene	**Amino Acid Change**	**Peptide**	**Allele**	**Percentile Rank**
Slc39a10	S286I	LPEHIGHEL	Dq	0.0225
Ttll4	Q454L	VPPSSLLPL	Dq	0.1367
Brinp3	T436P	CPAFLPCTV	Dq	0.2119
Cep76	P158A	VPCACEADF	Dq	0.4240
Atp9a	I216F	EPNIDFHNF	Dq	0.4662
Fam83f	Q4L	VPALPTESL	Dq	0.1392
Emc1	H307L	SHYALLHYL	Dq	0.2106
Cnot10	A543P	VPLALGDNL	Dq	0.0063
Fam13b	D766H	QEKLARHL	Kq	0.1266
Setbp1	N1160Y	HDYLSGLF	Kq	0.2688
Pcdh18	M631I	NEENIFII	Kq	0.1341
Cpt1c	Q29H	HEIYLCAL	Kq	0.3203
Trip4	Q423L	HQHQLRIL	Kq	0.3234

625 **Supp. Table 2: List of filtered peptide candidates for CIT6 neoantigens.** List of all neoantigen

626 peptide candidates that met the criteria specified in Fig. 4A. Percentile ranked based on

627 NetH2pan algorithm.

628

629

Supp. Table 3: List of Antibodies and Conjugated Fluorophores used for Flow Cytometry Analysis

Target	Fluorophore	Clone	Dilution	Manufacturer	Catalog #
B220	BUV661	RA3-6B2	1:200	BD Biosciences	612972
CD11b	BV711	M1/70	1:100	BioLegend	101242
CD11c	BV605	N418	1:100	BioLegend	117334
CD16/CD32 (FcR Block)	N/A	2.4G2	1:167	Tonbo	70-0161-U500
CD3e	BUV395	145-2C11	1:62.5	BD Biosciences	563565
CD4	BUV563	GK1.5	1:200	BD Biosciences	612923
CD44	BV785	1M7	1:200	BioLegend	103059
CD45	AlexaFluor700	30-F11	1:400	BioLegend	103128
CD62L	FITC	MEL-14	1:200	Invitrogen	11-0621-81
CD8a	BV570	53-6.7	1:200	BioLegend	100739
CD8a	BV785	53-6.7	1:200	BioLegend	100750
F4/80	APC	BM8	1:100	BioLegend	123116
FoxP3	PE-Cy7	FJK-16s	1:50	eBioscience	25-5773-82
Live/Dead	NIR	N/A	1:1000	Invitrogen	L34976A
Ly6C	BV650	HK1.4	1:200	BioLegend	128049
Ly6G	PE-CF594	1A8	1:200	BD Biosciences	562700
MHCII	PE-Cy7	M5/114.15.2	1:400	BioLegend	107630
PD-1	BV605	29F.1A12	1:100	BD Biosciences	135220
TIGIT	BV421	1G9	1:100	BioLegend	142111
Tim3	APC	RMT3-23	1:100	BioLegend	119705

630 **Supp. Table 3: List of antibodies used for flow cytometry analysis.** All antibodies, clone

631 number, and conjugated fluorophores for antibodies used for flow cytometry.

632

633